Journal of Manufacturing Processes 121 (2024) 35–50

Contents lists available at ScienceDirect

Journal of Manufacturing Processes

journal homepage: www.elsevier.com/locate/manpro

Research article

Validation of an experimentally-based heat source for flash heating modeling of directed energy deposition: Systematic study of process and simulation parameters

Alberto Santi [a,*], Mohamad Bayat [a], Venkata Karthik Nadimpalli [a], Alberto Fabrizi [b], Franco Bonollo [b], Jesper Henri Hattel [a]

[a] Department of Civil and Mechanical Engineering, Technical University of Denmark, Building 425, Kgs. Lyngby, 2800, Denmark
[b] Department of Engineering and Management, University of Padova, Stradella S. Nicola 3, Vicenza, 36100, Italy

ARTICLE INFO

Keywords:
Directed energy deposition
Thermal modeling
316L
Finite element method
Heat accumulation

ABSTRACT

Computational prediction of the temperature history during directed energy deposition (DED) is a fundamental input for the subsequent numerical analysis of microstructural characteristics and thermomechanical response. In order to allow for industrial implementation of such simulations, the development of computationally efficient methods taking advantage of multi-scaling techniques is needed. This work provides a new formulation for the flash heating (FH) method to be applied when modeling DED. As with other FH methods, this formulation ensures energy conservation when defining the volumetric heat source term, however, in the present case, the actual deposited cross-sectional area obtained from experiments is used instead of hatch spacing and layer thickness as usually done in FH methods for laser powder bed fusion (LPBF). A new feature of the model is that the high-resolution cross-sectional area of the multi-layer geometry is extracted from optical micrographs, resulting in a curvilinear top surface of every track. The method is validated through comparison with experimental monitoring data and provides valuable information regarding cooling rates, development of the molten area, and heat accumulation when varying process parameters within relevant limits. The influence of varying simulation parameters, such as the partitioning of the geometry and the time used for heating (contact time), on computational cost and accuracy is moreover studied. It is found that a very short contact time is mandatory to ensure the melting of the geometry and, consequently, the proper evaluation of cooling rates and thermal gradients.

1. Introduction

Predicting production outcomes for metal additive manufacturing (MAM) techniques is a time-consuming and expensive task, hindering an extensive industrial implementation of this class of manufacturing processes [1]. The complexity stems from the several process parameters to be set, the limited amount of materials available for MAM, and the limited knowledge of the physical phenomena taking place during the process [2]. Monitoring techniques are one of the main tools used for such purpose [3]; however, many are still under development, and some of them come with limitations on what is actually possible to measure without compromising the produced part. This is where computational tools are able to give extra input, providing an inexpensive evaluation of the manufacturability of a component without needing to produce and find a way to measure hard-to-evaluate quantities like e.g. residual stresses.

Powder-based directed energy deposition (DED) allows for 3D-printing of large metallic components based on a working principle taken from metal welding: the powder is fed by a co-axial or off-axis nozzle, melted by a laser source, and subsequently deposited and re-solidified on top of a baseplate. In this way, it is possible to build new components through layer-by-layer deposition, leaving enhanced design freedom as compared to other conventional processes [4]. DED presents several similarities to powder bed fusion (PBF), which produces smaller components by selectively melting powder lying on the build table or bed. Therefore these two processes are typically presented together when dealing with modeling, as nearly identical physics are involved [5].

Due to limited computational resources, it is not possible to include all the occurring physical phenomena during MAM in the simulation, and, as a result, only relevant physical phenomena with a focus on the

* Corresponding author.
E-mail address: albsa@dtu.dk (A. Santi).

https://doi.org/10.1016/j.jmapro.2024.05.026
Received 15 January 2024; Received in revised form 4 April 2024; Accepted 8 May 2024
Available online 17 May 2024
1526-6125/© 2024 The Author(s). Published by Elsevier Ltd on behalf of The Society of Manufacturing Engineers. This is an open access article under the CC BY license (http://creativecommons.org/licenses/by/4.0/).

prediction of a specific class of defects and on a specific length-scale are considered. Heat transfer is taken into account in most of these models, as MAM processes typically function based on the fusion and melting of the feedstock material, leading to melt pool formation, followed by cooling. The final microstructural pattern, the potential presence of key-hole or lack-of-fusion porosities, and residual stresses are governed by the complex fluid flow, solidification, and cooling stage. The central role of the thermal conditions is deeply addressed in [6,7]. Bayat et al. [8] provided a classification of the different modeling techniques applied to MAM based on their length-scale and the main output of the model. The three length-scales are as follows: micro-scale models focus on the microstructural evolution [9], meso-scale (or deposition-scale) models' computational domain is within the vicinity of the melt pool [10], and finally, part-scale models simulate field variables in the entire part — although often by means of proper process multi-scaling techniques.

At part-scale, thermal models predict cooling rates and possible temperature build-up (residual heat and overheating) in the sample during the process [11–14], which in turn could lead to the coarsening of the microstructure and cause decreased hardness [15,16]. In thermo-mechanical models, thermal models provide temperature as input for the mechanical model through a weak coupling to obtain residual stresses and distortions in weakly coupled thermo-mechanical models [17–29]. When applied to MAM, the idea behind these models is to: (1) find the best set of process parameters and scanning patterns leading to minimum distortion/residual stresses [21], (2) to redesign the components compensating for the predicted distortions [26,30], or (3) to evaluate the effects of post-production heat treatments on the thermo-mechanical conditions [27].

Thermal and thermo-mechanical part-scale models are typically based on the finite element method (FEM), taking into account only the conduction of heat within the geometry, as including fluid dynamics effects such as convection, evaporation or the Marangoni effect would strongly increase the required computational time. The final geometry is given as an input and not generated during the simulation. The material deposition is replicated by the element birth-and-death technique, where the elements are activated step-by-step according to when they should be deposited [31], or by the quiet element approach, where all the elements are active from the beginning but the ones which should not be active yet, present null material properties [32].

There are several ways to simulate the laser's thermal impact on the material. Simulating the laser as a moving heat source [22,33–35], with a certain energy distribution over the area of the laser diameter [36,37] is one way of capturing this. Even if this approach turns out to be the most reliable one at meso- or deposition-scale, it is computationally heavy and infeasible when the domain covers several tracks and layers. For these reasons, the method is usually compromised with adaptive remeshing techniques to reduce the number of elements and hence the simulation time [38–40].

Process multi-scaling techniques are a key solution to circumvent the high computational requirements seen in the moving heat source approaches. Several different process multi-scaling techniques have been proposed in the MAM literature. Material lumping is a key feature that all process multi-scaling techniques have in common. Here, elements are lumped together, allowing for a large time step as compared to the moving heat source techniques, where activation of the elements happens continuously with the movement of the laser. Hodge et al. [23] executed heat source agglomeration by considering a laser diameter and layer thickness being 20 times bigger than the real-life case. On the other side, Zaeh et al. [41] proposed to heat up parts of each layer (scanning areas) through a volumetric heat source. This idea was further developed in Zhang et al. [18] where the volumetric heat source is applied to a lump of layers (meta-layer) that are heated up all together at the same time, defining what is currently denoted the flash heating (FH) method. Finally, a modified version of the inherent strain method, which was initially applied for welding problems [42], has been implemented for purely mechanical analysis of MAM [43,44]. In the most recent version, the modified inherent strain method is coupled with FH for more realistic stress predictions in high-throughput MAM processes e.g. wire arc additive manufacturing [24].

The present paper proposes a new formulation for the FH method applicable to the powder-based DED process. In [25], a theoretical procedure for FH, as well as the so-called sequential flash heating (SFH), for LPBF is presented, in which the volumetric heat source applied to every meta-layer is obtained based on process parameters. Such procedure, as will be shown later in the paper, cannot be applied to DED, as there is a big contrast between the length-scales of DED and LPBF reflected in the part width and hatch spacing — hence necessitating a somewhat different approach. The proposed FH method is validated and supported through experimental data and applied to different sets of process parameters.

The FH method can be implemented in a couple of different ways, discussed below, via adjusting the contact time, i.e., the parameter that defines the amount of time over which the thermal energy is released into the deposited material. In some studies, the contact time is defined as the ratio between the laser beam diameter and the scanning speed [28,29], as this would provide the actual amount of time in which a representative area of the material gets heated by the laser. The contact time spans from very small values [18,25], in the order of milliseconds, to a comparatively longer period i.e. equal to the deposition time (defined as the real experimental time used to deposit the layers composing the meta-layer), and this would provide a way for gradual heating of the material instead (denoted gradual heating, GH) [14]. The impact of this modeling parameter on the reliability and run-time of the FH model is, however, rather unknown, and in this paper, we seek to study the effect of contact time on the thermal conditions during the DED process.

Moreover, in part-scale models described in the MAM literature, the geometry of the deposited tracks in DED processes is predominantly assumed to be flat and have parallelepiped shape [45–47], and this is quite far from real conditions, as it is well established from experiments that the cross-sections of DED-printed layers present curved surfaces (also called free surfaces) [48,49]. Therefore, considering a nominal geometry instead of the real one can lead, in a simulation environment, to a wrong estimation of the temperature field due to a different amount of material deposited per track or just a different distribution of it. Also, adopting the nominal geometry complicates the evaluation of overlapping between neighbor tracks [28]. Some attempts have been made to analytically derive the cross-sectional shapes of the track through curvilinear field equations depending on process parameters [50–55], but these are still limited to a few layers. In this work, the cross-sectional geometry of the component analyzed in the simulations is based on observations made through an optical microscope (OM), capable of providing reliable information on the amount of material that gets deposited and on its shape.

The paper is structured as follows: firstly, a description of the experimental setup is provided, comprising the equipment used for production, its monitoring, and subsequent material characterization. Secondly, the numerical model is described, explaining which governing equations and corresponding boundary conditions are considered. Finally, the simulation results are provided and discussed in context with the experimental findings.

2. Experimental setup

Samples of stainless steel AISI 316L have been produced through a powder-based DED process (setup shown in Fig. 1). The system uses a GTV multi-jet nozzle (PN6625) mounted on a 5-axis KUKA robotic arm. The particle size distribution of the powder is reported in Table 1. Thermal energy for melting the powder particles is provided through a collimated diode laser (Laserline LDF 16000-60) properly focused on the baseplate, made of the same material as the powder

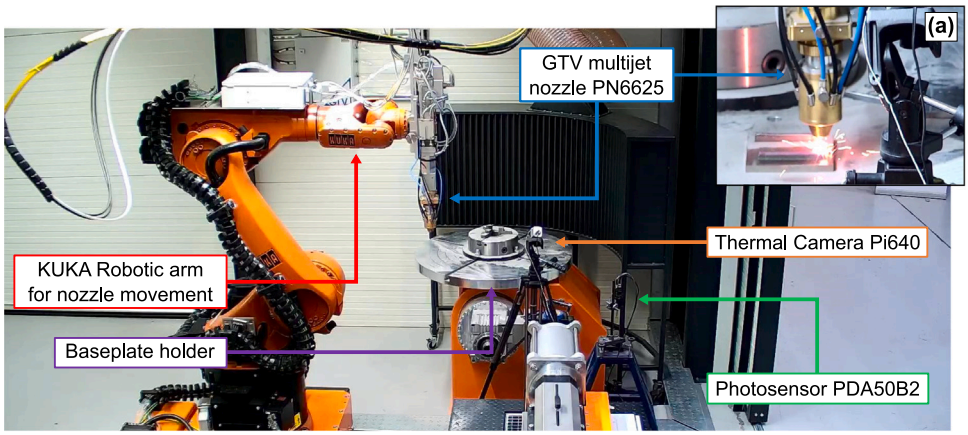

Fig. 1. View of the experimental setup together with online monitoring equipment. (a) Zoom in during the DED process.

Table 1
Particle size distribution of 316L powder.

Particle size [μm]	>106	106–90	90–75	75–63	63–53	53–45	45–38	<38
%	0.0	4.1	27.2	39.5	21.0	7.1	1.0	0.0

Table 2
Process parameters used for the different samples. The P/v representing the linear energy density input ($LED = P/v$) is also reported.

Sample tag	P [W]	v [mm/s]	P/v [J/mm]
L (low LED)	1500	25.00	60
N (nominal LED)	2100	16.67	126
H (high LED)	2700	8.33	324

deposited. The laser diameter is 3 mm. Argon is used as a shielding gas. These experiments aimed to investigate the influence of the volumetric energy density input VED on the final components. This parameter is calculated as follows:

$$VED\ \left[\mathrm{J/mm^3}\right] = \frac{P}{Gv} \tag{1}$$

where P [W] is the laser power, v [mm/s] the laser scanning speed, and G [mm^2] a geometrical constant. For LPBF, $G = H\delta$, where H [mm] is the hatch spacing and δ [mm] is the layer thickness. For DED, $G = A_t$ where A_t [mm^2] is the single-track cross-sectional area as it will be described in the subsequent Section 3.5.

Several parts have been printed in the experimental campaign; however, this study is limited only to three of them of which the process parameters are reported in Table 2.

Both single tracks and multi-layer samples are produced for each set of process parameters. All the multi-layer parts are made of 14 layers, each having three tracks deposited in alternating directions, with an overlapping distance of 1 mm (considering a laser diameter of 3 mm, $H = 2$ mm) as shown in Fig. 2a. Baseplates have a square shape with a size of 120 mm × 120 mm and a thickness of 9 mm. On each of these, two samples are deposited (Fig. 2b). The three samples considered in this study were the first to be printed in three different baseplates to avoid any noise from the previously deposited part in the same baseplate.

2.1. Monitoring and characterization techniques

The following online monitoring equipment was installed during production:

- A mineral-insulated K-type thermocouple on the sample N with a 3 mm sheath outer diameter. The position of the thermocouple in the baseplate is shown in Fig. 2c. The thermocouple wires are set in a drilled hole of 0.5 mm and kept in place through an appropriate thermal paste.
- An infrared thermal camera (Thermal imager OPTRIS Pi640). This equipment provides the temperature development in every pixel of the recorded video based on the infrared (IR) emissions from the targeted bodies. Implementing such equipment is quite complex, as it cannot stand close to the sample due to melt spattering, which can ruin the camera. Therefore, this is kept quite distant, leading to every pixel including a bigger region. Furthermore, the temperature range for the used equipment is 200–1500 °C, while the experiments go below and beyond this range.
- A photosensor (PDA50B2 Ge Switchable Gain Amplified Detector, 800–1800 nm, 510 kHz BW, 19.6 mm^2, Universal 832/M4 Taps). When emissions with wavelengths between 800–1800 nm are detected, this sensor outputs a voltage value dependent on the waves' intensity. This looks at the whole deposition, not at a specific point.
- An in-axis camera. Coaxial to the laser beam and perpendicular to the baseplate, it visualizes the melt pool deposited from the top, monitoring its dimension and shape based on the light reflection.

After production, the parts are cut in the middle of their length, along the yz-plane, to investigate their cross-sections. The preparation of the samples followed the standard procedure for microstructural characterization. The following characterization instruments are used to analyze the parts:

- An optical microscope (Leica DM6). The samples are inspected both before and after etching with glyceregia [56]. The investigation before etching helps visualize the overall cross-section dimensions, shape, and potential macro-porosities; the one after, on the other hand, is executed to see the melting lines and distinguish the different tracks deposited.
- A field-emission scanning electron microscope (FEI Quanta 250). The micrographs are acquired using back-scattered electrons with the electron channel effect contrast imaging (ECCI) mode to distinguish grains with different orientations [57]. Grain size and morphology can be evaluated in this way.
- A microhardness tester (FutureTech FM810). Measurements along the cross-sections are executed to evaluate hardness variations along the build direction. A load of 200 g with a dwell time of 10 s is applied for all the measurements (two profiles per sample).

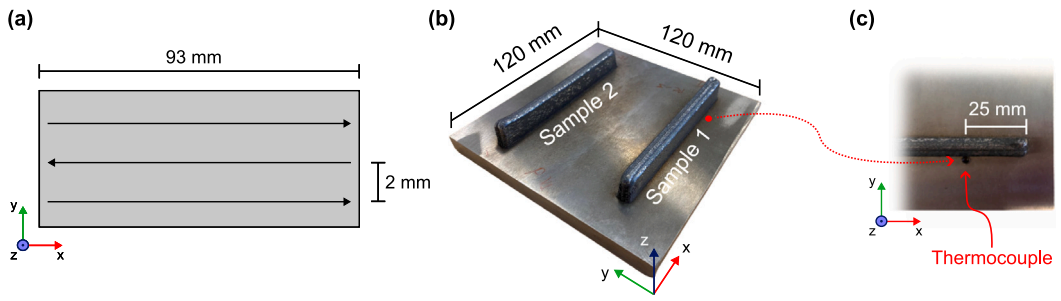

Fig. 2. (a) Scanning pattern and hatch size. (b) Build plate after production. Only the first samples produced in each baseplate are considered (Sample 1). In this figure, Sample 1 corresponds to L. (c) Position of the thermocouple for Sample N. The reported coordinate system coincides with the one used in the FEM simulations.

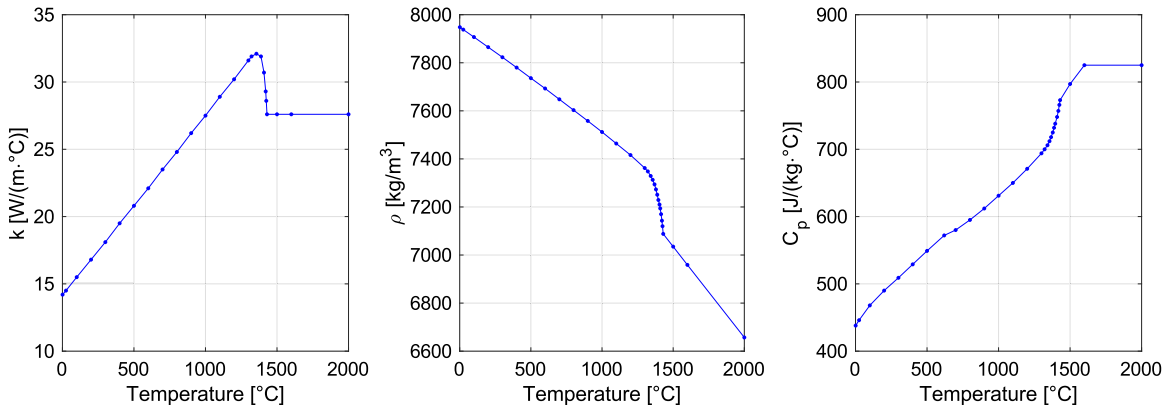

Fig. 3. Temperature-dependent thermophysical material properties of AISI 316L [58].

3. Numerical modeling

3.1. Transient thermal analysis

To obtain the temperature field development during the DED process within the baseplate and printed material, the well-known transient heat conduction equation is solved through FEM at part-scale [17]:

$$\rho \cdot C_p \cdot \frac{\partial T}{\partial t} = \frac{\partial}{\partial x}\left(k \cdot \frac{\partial T}{\partial x}\right) + \frac{\partial}{\partial y}\left(k \cdot \frac{\partial T}{\partial y}\right) + \frac{\partial}{\partial z}\left(k \cdot \frac{\partial T}{\partial z}\right) - \rho \cdot \Delta H_{sl} \cdot \frac{\partial f_{liq}}{\partial t} + \dot{Q}''' \tag{2}$$

where ρ [kg m^{-3}] is the material density, C_p [J kg^{-1} °C^{-1}] is the specific heat capacity, k [W m^{-1} °C^{-1}] is the material conductivity, ΔH_{sl} [J kg^{-1}] is the latent heat of fusion, f_{liq} is the liquid fraction and $\dot{Q}'''$ [W m^{-3}] the volumetric heat source related to the FH implementation discussed in Section 3.4. Temperature-dependent material properties are implemented, also considering the change of behavior due to melting and solidification (Fig. 3). f_{liq} is assumed to have a linear behavior between the solidus and liquidus temperature, respectively T_{sol} = 1322 °C and T_{liq} = 1430 °C, during which the amount of latent heat released is equal to ΔH_{sl} = 272 kJ kg^{-1}.

3.2. Thermal boundary conditions

Except for the bottom, all surfaces of the baseplate as well as the surface of the deposited material are exposed to air convection and radiation. The thermal boundary condition is expressed as [17]:

$$-k\frac{\partial T}{\partial z} = h_{amb}\left[T - T_{amb}\right] + \varepsilon \cdot \eta\left[T^4 - T_{amb}^4\right] \tag{3}$$

where h_{amb} = 15 W m^{-2} °C^{-1}, ε = 0.4 [10] and η = 5.67·10^{-8} W m^{-2} °C^{-4} are respectively the air heat transfer coefficient (free convection, assumed to be constant throughout the whole simulation [20, 27,46]), the surface emissivity of AISI 316L, and the Stefan–Boltzmann constant. The ambient temperature T_{amb} = 23 °C is uniformly assigned to the baseplate before the deposition, as detected by the thermocouple.

The bottom of the baseplate is in contact with a supporting structure, through which heat can conduct and be dissipated. An additional boundary condition is prescribed to consider this contribution, where an equivalent heat transfer coefficient h_{cool} is calibrated and validated.

3.3. Deposition geometry

To implement realistic overlapping of the deposited tracks, pictures of the cross-section obtained through the OM are used to achieve the same shape in the simulated geometry (Fig. 4a). For the geometry of each track, in approach 1 shown in Fig. 4b, circular arcs are manually drawn to realistically replicate the free surfaces whilst also allowing identical areas for each track's cross-section and overlapping neighbor tracks of 1 mm. These do not match with the lines visualized in the OM picture, manually drawn in the approach 2 geometry in Fig. 4c, as remelting of previously deposited tracks takes place during experiments, causing the upper layers to look like they have more material deposited as compared to the bottom ones. Obviously, this does not hold if powder feed and catching efficiency [59] are considered constant. The cross-section is then "extruded" for the whole deposition length of 9.3 cm and positioned in the baseplate (Fig. 4d). The same approach is used for all the analyzed geometries (Fig. 5). Meshing is done with DC3D8 elements, which are refined close to the deposition.

3.4. Issues in the implementation of the FH LPBF procedure for DED

The idea behind the FH method is to homogeneously heat up a lump of several 3D printed layers, denoted meta-layers, through a volumetric heat source $\dot{Q}'''$ derived from process parameters. Such thermal energy is applied in a much shorter time as compared to the deposition time Δt_d [s], and it is referred to as the contact time Δt_{cont} [s]. From [25],

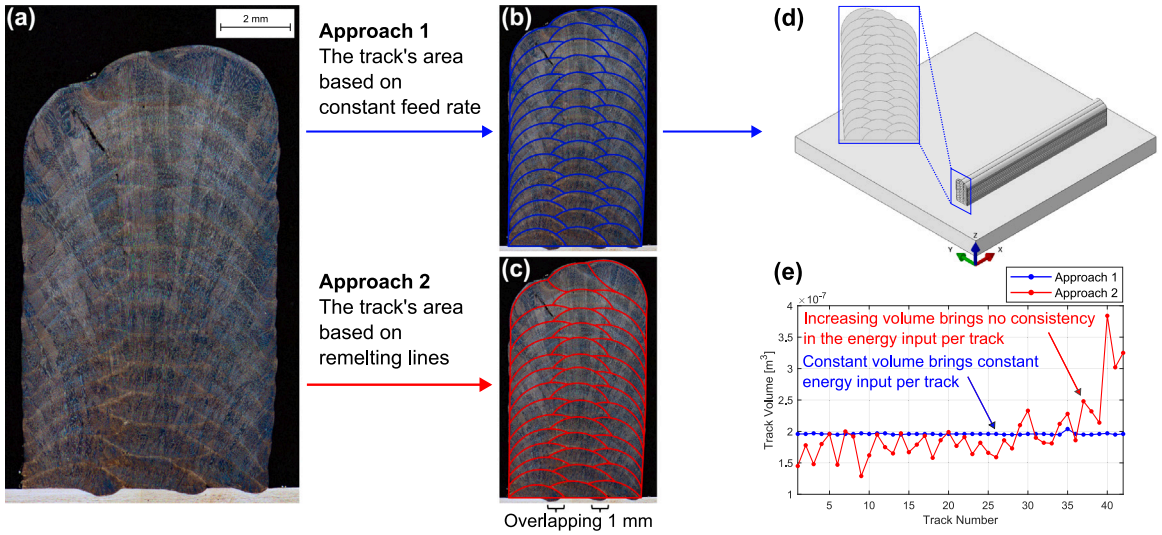

Fig. 4. (a) Optical microscope picture of the cross-section of the sample denoted N after etching. (b–c) The geometry of the cross-section is modeled with circular arcs. Approach 1 is based on constant volume (b), while Approach 2 on the melting lines visualized after etching (c). (d) Final geometry of deposited tracks, based on Approach 1. (e) Development of the volumes as a function of the track number, with the two different approaches. Approach 1 shows constant volume per track, as defined. Approach 2 shows an increase in volumes at the last tracks, which is a consequence of the track-wise heat accumulation.

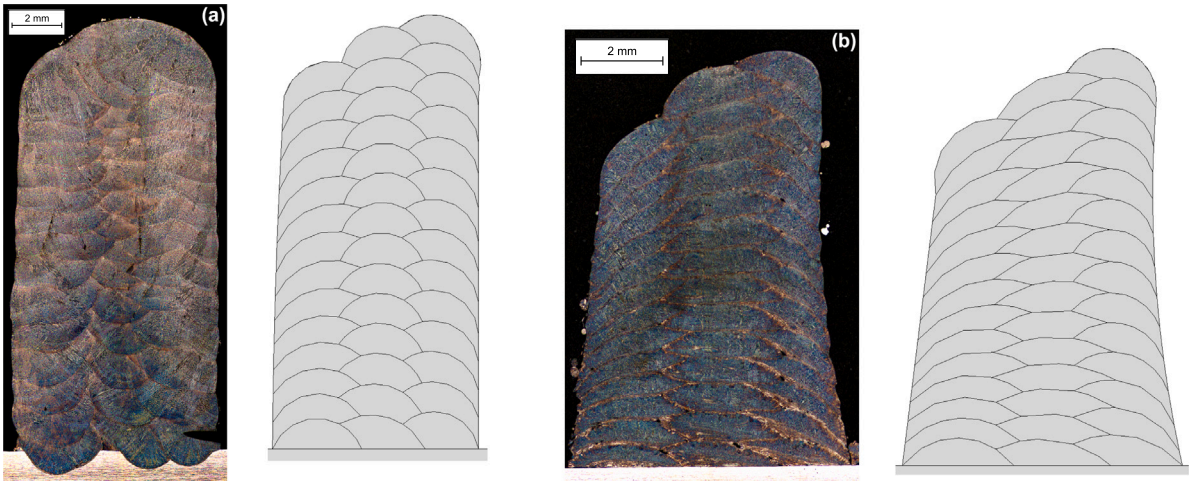

Fig. 5. Cross-sections from OM measurements of the samples after etching with corresponding manually extracted geometry for simulations. (a) shows sample H, (b) sample L. Discrepancies between numerical and experimental geometries are due to ensuring constant volume per track.

the following equation is used to evaluate $\dot{Q}'''$ input for the FH method in LPBF:

$$\dot{Q}''' = \frac{U_\delta \cdot (\Delta/\delta)}{\Delta t_{cont} \cdot V} \tag{4}$$

where U_δ [J] is the energy input per layer, δ [mm] is the actual layer thickness, Δ [mm] is the meta-layer thickness, and V [mm^3] is the volume of the deposited meta-layer. The value of U_δ is given by

$$U_\delta = \xi \cdot P \cdot \Delta t_d \tag{5}$$

where ξ is the laser absorptivity, assumed to be constant as done in other previous works at meso-scale level [60–63]. Δt_d [s] is the deposition time, obtained from

$$\Delta t_d = \frac{L}{v} \cdot n_{track} = \frac{L}{v} \cdot \frac{w}{H} \tag{6}$$

where L [mm] is the track length, n_{track} the number of tracks per layer, and w [mm] the layer width. Inserting Eq. (5) and Eq. (6) in Eq. (4), the relationship between the volumetric heat source and process parameters is finally obtained:

$$\dot{Q}''' = \frac{\xi \cdot P}{H \cdot v \cdot \Delta t_{cont} \cdot \delta} \tag{7}$$

Eq. (7) holds for LPBF but does not for DED. This is because Eq. (6) assumes that $n_{tracks} = w/H$. This expression never provides the exact integer value, as one should have no overlapping to obtain the precise number of tracks. Therefore, some decimal digits are present, bringing an overestimation of n_{tracks} and subsequently of $\dot{Q}'''$. The approximation works well for LPBF as $H \ll w$, having the hatch spacing in the order of micrometers and the part width within millimeters or centimeters. This means that the number of tracks is high, in the order of hundreds or thousands, and a wrong estimation of the value in the decimals brings a negligible error in $\dot{Q}'''$. On the other hand, both H and w are in the same order of magnitude for DED. If we analyze sample N, having a width of 7 mm and a hatch spacing of 2 mm, the number of tracks estimated with such a formula will be 3.5 which will result in a subsequent overestimation of $\dot{Q}'''$ of 16.67%. This error is connected to the overlapping of neighbor tracks: the difference between the calculated number of tracks and the actual one corresponds to the

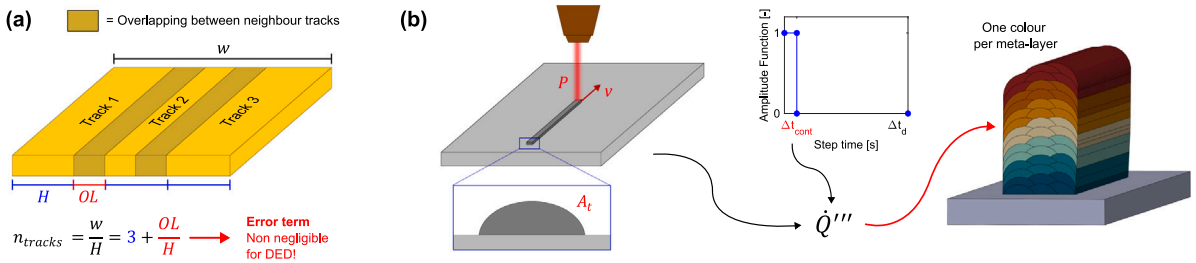

Fig. 6. (a) Representation of three adjacent overlapping tracks. The evaluation of the number of tracks through the formulation introduced in [25] includes an error term that linearly depends on the ratio between the overlapping OL and part width w. (b) Representation of a DED process with the simulation parameters needed (in red) to define the volumetric heat source. This is then applied to the geometry (as indicated by the red arrow), which is discretized in meta-layers (here shown in different colors) activated one after the other. (For interpretation of the references to color in this figure legend, the reader is referred to the web version of this article.)

relative overlapping between two tracks (Fig. 6a). This error is too big to be neglected, so a new procedure is required.

3.5. FH implementation for DED

Focusing only on a single track ($\Delta/\delta = 1$), the deposition time can be evaluated as

$$\Delta t_d = \Delta x_t / v \tag{8}$$

where Δx_t [mm] is the length of the deposited track. If such a term is introduced in Eq. (6), the new relationship between process parameters and the volumetric heat source is found for DED through Eq. (4) (Fig. 6b):

$$\dot{Q}''' = \frac{\xi \cdot P}{A_t \cdot v \cdot \Delta t_{cont}} \tag{9}$$

where A_t [mm^2] is the cross-sectional area of a deposited track.

The main difference between Eqs. (7) and (9) can be found in the denominator: for LPBF, the geometrical inputs are given by H and δ, while instead for DED it is condensed in A_t only. In both cases, preliminary knowledge from experiments is required: for the LPBF case, the layer thickness needs to be evaluated a-priori, while for the DED case, it is the cross-sectional area of a single-track deposition that needs to be known in advance. This is why, in this case, single-track experiments are executed to obtain the cross-sectional area of the depositions for the different sets of process parameters employed in the experiments.

An alternative formulation for $\dot{Q}'''$ can be obtained if the mass flow rate is known. The mass flow rate $\dot{m}$ is defined as

$$\dot{m}\,[g/s] = A_t \cdot v \cdot \rho \tag{10}$$

which allows to obtain a new formulation of the volumetric heat source that does not necessitate prior knowledge of the cross-sectional area of an ST experiment:

$$\dot{Q}''' = \frac{\xi \cdot P \cdot \rho}{\dot{m} \cdot \Delta t_{cont}} \tag{11}$$

This alternative equation can be used only if proper deposition of the powder is ensured: if too much energy is provided by the laser, spattering can occur, and, on the other hand, a small energy input can cause having unmelted powder. In both these cases, $\dot{m}$ would not provide reliable information about the material actually deposited and the more reliable information of the cross-sectional area should be used. For the experiments under analysis in this work, Eq. (9) was used as the value of $\dot{m}$ is unknown, but kept constant for the different experiments

Eqs. (9) and (11) can be used with every kind of discretization of the geometry: meta-layers, layers, tracks, or parts of them. To use a homogenized term, from this point, all such discretizations are denoted patches. For LPBF, one would consider meta-layers solely for computational reasons. The energy input term is given per unit volume and ensures energy consistency, i.e. the input of the right amount of energy. Time consistency is ensured by activating the patches at the right time and in consistency with real-life tests, according to the element birth-and-death technique. Based on the scanning pattern adopted, an additional 1.25 s is taken into account between the deposition of two layers and 0.25 s between the deposition of tracks within the same layer. For the deposition of each patch, two steps are considered: one where the volumetric heat source is applied to it (heating), and a second one where such patch cools down until the next patch needs to get deposited. The initial time increment is set to one-tenth of the contact time for each step, with the size of subsequent increments being allowed to increase depending on the convergence of the field equation.

Simulations are developed through in-house built Python codes and executed in Abaqus/CAE 2018. All run on 20-core High Performance Computing machines at DTU.

4. Results and discussion

4.1. Thermal validation

The cross-sectional area A_t of the three sets of process parameters evaluated from experimental OM measurements are reported in Fig. 7. These also correspond to the areas obtained by partitioning the build geometry equally, as shown in Figs. 4 and 5. The geometry of the tracks varies strongly at different energy densities, in agreement with what is found in [64]. The track width stays mostly constant given the fixed laser diameter, while height and dilution increase when increasing the energy density, as expected.

The only two unknown variables are ξ and h_{cool}, which must be calibrated against the experiments. Such calibration is executed based on the experimental data given by the thermocouple installed during the production of sample N. The correct choice of these two variables, ξ and h_{cool}, will ensure the correct maximum temperature followed by realistic bulk cooling afterward, respectively.

This first validation is executed with very refined patching and meshing where each layer is discretized into 24 patches (3 tracks of 8 patches), and a total number of 427 184 elements is used. Fig. 8 shows the temperature–time curves obtained both with approach 1 (equal volume deposited per each track) and 2 (resembling melting lines visualized through OM) presented in Fig. 4b. Approach 1 leads to a good agreement with the experimental curve, while approach 2 overestimates the temperature in the last layers. This overestimation occurs as the volumetric energy source is applied to bigger volumes for the upper layers, as the tracks composing these have an increased volume as shown in Fig. 4d. From a modeling perspective, if process parameters are not modified in the process, the same energy should be provided per each track deposited, and that is where approach 2 fails in replicating the experimental data. As earlier pinpointed, the apparent increased volume per track is not a consequence of different deposition rates but rather of the increased heat accumulation in the upper layers. On the other side, approach 1 deposits the same amount of material in each layer, providing an identical heat input for each and obtaining the

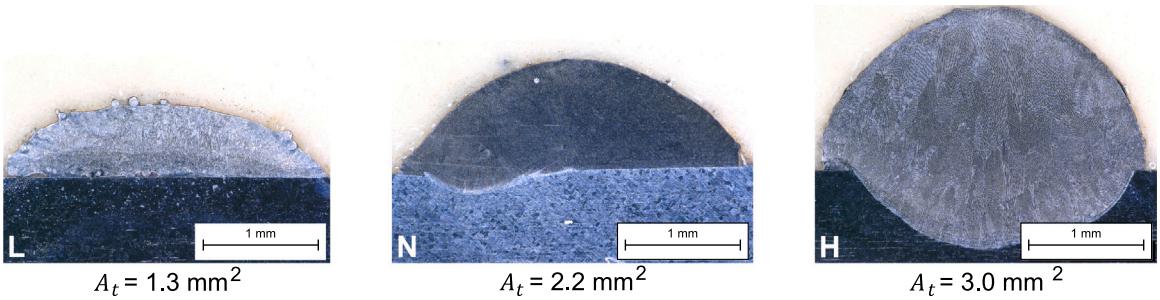

Fig. 7. OM of single track deposition for the three different sets of process parameters given in Table 2. The estimated cross-sectional area is reported below each picture.

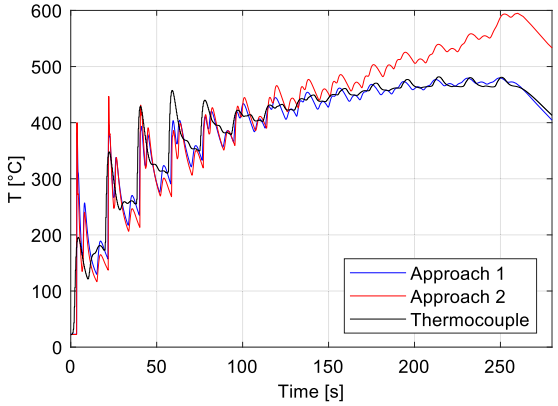

Fig. 8. Comparison between experimental and numerical temperature–time curves at the thermocouple position.

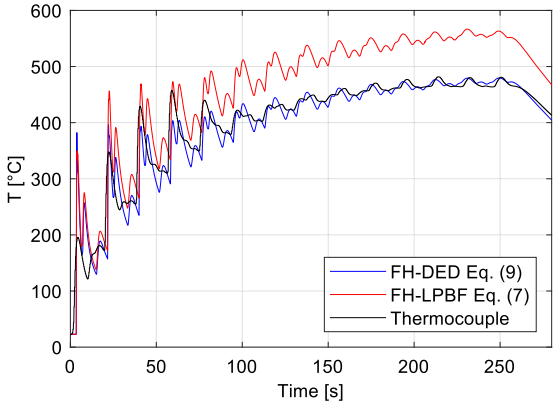

Fig. 9. Comparison between experimental and numerical temperature–time curves at the thermocouple position. The two numerical curves are obtained using different volumetric heat source values, obtained with the FH-DED and FH-LPBF equations respectively.

desired validation with the experiments. For these reasons, approach 2 is not considered for modeling, and the geometry of approach 1 is used.

The energy consistency of approach 1 is achieved with h_{cool} = 150 W m^{-2} °C^{-1}, and ξ = 0.362. This is found to agree with what was concluded in [63], namely that a constant absorptivity of 0.35 gives a good match between experiments and numerical results. Time consistency can also be concluded from this comparison since experimentally and numerically obtained peaks coincide with good agreement. Further confirmations can be found as supplementary material in Appendix A.

The necessity of using the FH-DED formulation for the volumetric heat source given in Eq. (9) instead of the FH-LPBF one of Eq. (7) is underlined by Fig. 9. In this picture, the temperature developments at the thermocouple are shown for two models using respectively the FH-LPBF and FH-DED equations for the volumetric heat sources. As expected, the model using Eq. (7) overestimates the temperature as the absorptivity has been calibrated to match with the curve given by Eq. (9). To achieve a match between the volumetric heat sources, the value obtained through Eq. (7) should be scaled down by 16.67%, bringing a decrease of the absorptivity to 0.302, which is underestimated compared to experimental measurements [65].

As a final validation, in Fig. 10, the maximum melt pool size is investigated for the last track deposited. This is compared with the nominal geometry used in the model (Fig. 10a) and with the geometry used in approach 2 in Fig. 4 based on the final melting lines visualized in the cross-section after etching (Fig. 10b). According to Fig. 10a, one can notice that, as expected in DED, remelting of previous tracks takes place, as the melt pool size is bigger than the amount of material deposited per track. At the same time, it is also seen that the numerical model is capable of effectively predicting the melting line positions, as shown in Fig. 10b, where the molten area coincides with the one drawn based on the melting lines visualized in the sample. Such an evaluation has not been found in previous literature, and this allows us to conclude that melting lines can be well predicted through well-calibrated purely conductive FEM thermal models.

Using the cross-sectional areas reported in Fig. 7, one could derive an estimation of the mass flow rate through Eq. (10). For the samples L, N, and H, the obtained values are 0.25 g/s, 0.28 g/s, and 0.19 g/s. It is not surprising to find a mismatch between these results, even if the same value should be expected: sample L was not provided with enough energy to ensure complete melting of the provided powder (one could also notice this from the surface of the cross-section within Fig. 7, where powder particles are not homogeneously sintered within the track), while sample H showed spattering during production. These considerations are also supported by the material reported in Appendix B, where the in-axis camera detects the phenomena just described.

4.2. Mesh sensitivity analysis

The influence of the number of elements is studied here to ensure mesh independence. Five different meshes of the deposition and baseplate are studied, ranging from refined to coarse element sizes, and here the same patching and contact time as employed in the validation case are used. All the models deposit the part with 8 patches per track within a contact time of 0.001 s. Table 3 gives the information on the model names and meshing. Fig. 11(right) shows the development of the root mean square error (RMSE) and run-time with respect to the number of elements. The RMSE is calculated by taking the temperature–time curves at the same position of the thermocouple and evaluating the difference among them, using the most refined model as a reference, according to the following formula:

$$RMSE\,[°C] = \sqrt{\frac{\sum_{i=1}^{N}\left(T_{i,REF} - T_{i,X}\right)^2}{N}} \tag{12}$$

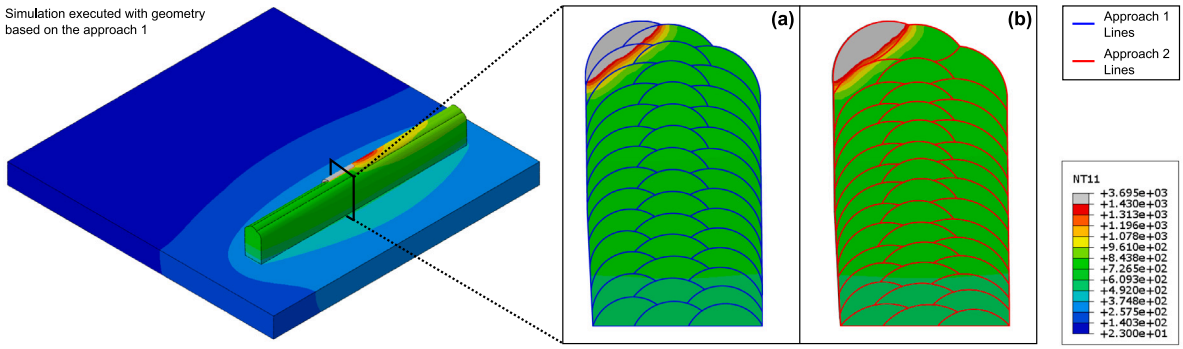

Fig. 10. Temperature contour at t = 251.6 s during printing of the last track. (a) Compares the contour plot with the simulation geometry (approach 1), showing a melt pool area bigger than the deposited track. (b) Compares it with the melting lines manually detected through OM (approach 2), showing a very good prediction of the molten volume from the numerical model. The temperature unit is degrees Celsius.

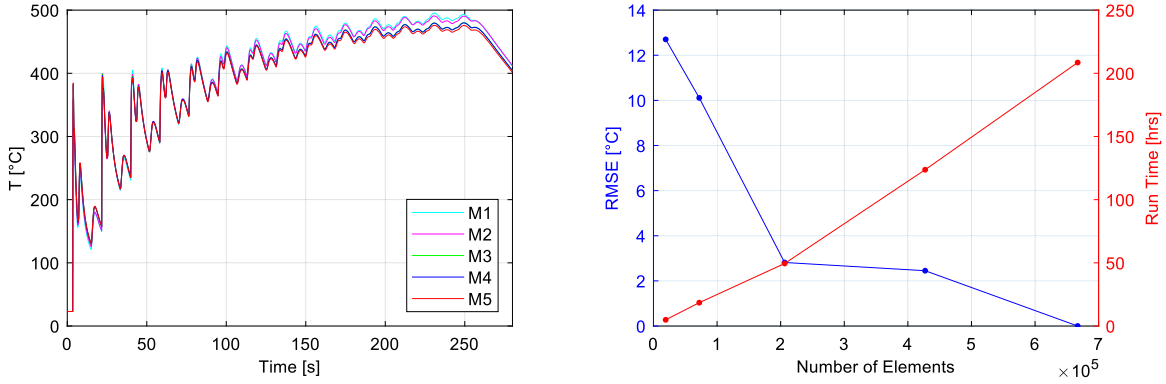

Fig. 11. On the left, temperature–time curves at the thermocouple position (shown in Fig. 2) of models with different numbers of elements. On the right, RMSE and run time development with an increasing number of elements.

Table 3
Models analyzed for the mesh sensitivity study.

Model name	Number of elements
M1	19 200
M2	72 000
M3	206 207
M4	427 184
M5	666 972

Table 4
Models analyzed for the parametric study on the number of patches.

Model name	Patch dimension	Patches per track
L7	7 layers	0.048
L2	2 layers	0.167
L1	1 layer	0.333
T	1 track	1
P2	0.5 track	2
P8	0.125 track	8

where $T_{i,REF}$ is the temperature detected by the model used as a reference (in this case, the one having the highest resolution, M5, as further refinement of the mesh would not change the result shown in Fig. 11), $T_{i,X}$ is the one detected by any of the other models, and N is the number of points collected over time. From the results in Fig. 11(left), it can be concluded that the models differ very little, with a general deviation of only 13 °C between the two extreme cases. One could then use the most coarse model to obtain a quick evaluation the temperature history during DED. However, in Fig. 12, one can notice a less precise contour plot in the cross-sections in the most coarse model, meaning that precise information on the molten volume might be lost in the process. The run-times are found to be almost linearly correlated to the number of elements used. For the rest of the discussions, run-times shown for the models will refer to the ones having an M1 mesh, while contour plots showing the temperature contours will come from models with identical settings, however having either M3 or M4 meshing.

4.3. Parametric analysis on FH simulation parameters

The two simulation parameters investigated in this section are the number of patches used per layer, and the contact time, respectively. These are process-independent parameters that can be tuned by the user.

In Table 4, a list of the analyzed models with different numbers of patches per track, along with their tags, is given. The built thermal models use the same meshing as model M1 and take the P8 model as a reference for RMSE evaluations. The temperature–time curves are now very different in terms of the number of peaks visualized and their position (Fig. 13a), but it is possible to see that the overall bulk temperature is not changed as the temperature builds up in the same way for all the models. When depositing a smaller number of patches, the peaks get higher given the bigger volume deposited per patch (and therefore more energy input) during Δt_{cont}. When comparing models with patching larger than a single track dimension, the number of fluctuations equals the number of patches getting deposited, and all are equidistant in time. In other words, when using patches smaller than a single track size, the number of peaks does not change anymore as they correspond to the number of tracks, but their position gets affected due to the scanning pattern effect (Fig. 13b). Model T shows equidistant peaks given the independence from the scanning pattern, whereas models with more refined patch dimensions depend on the scanning pattern, resulting in unequal distances between the peaks.

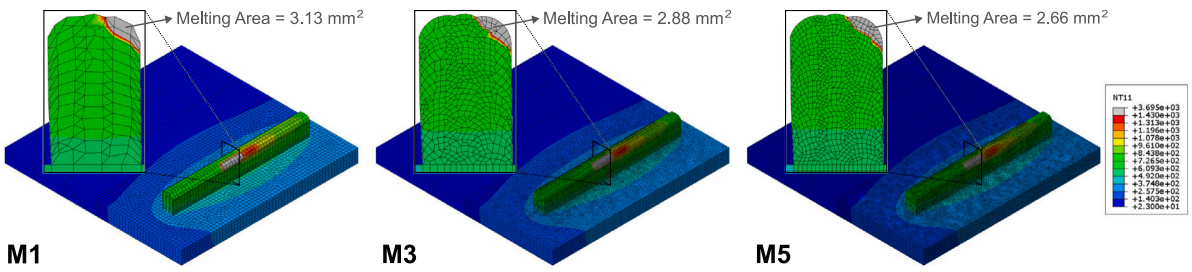

Fig. 12. Contour plots at $t = 239.94$ s with increasing number of elements. The temperature unit is degrees Celsius. The melting area is also reported, showing an improvement in its evaluation with an increased number of elements.

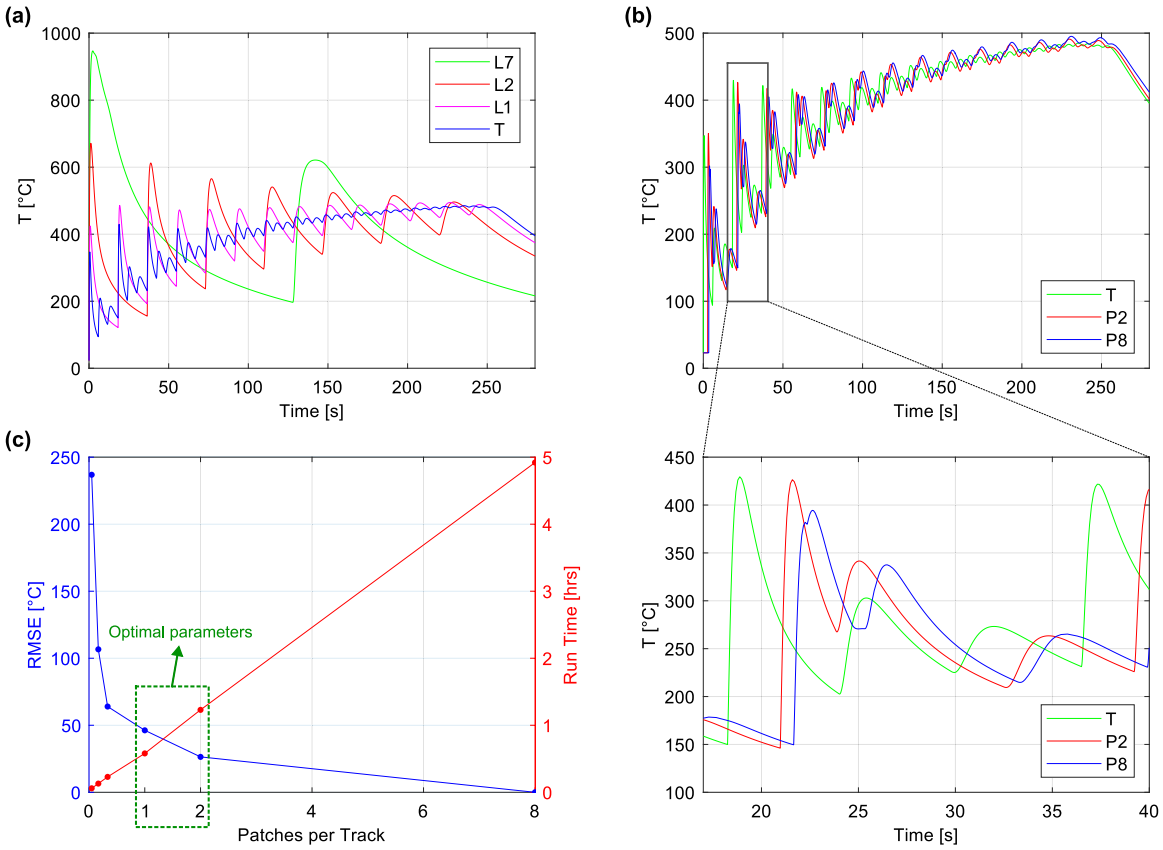

Fig. 13. (a) Temperature–time curves at the thermocouple position for models having different patching (above track dimension). (b) Temperature–time curves at the thermocouple position for models having different patching (below track dimension), with zoom up on the deposition of the second layer. (c) RMSE and run time development with an increasing number of patches per track (given in Table 4), indicating the recommended range of parameters to achieve the best trade-off between accuracy and computational cost.

Such temperature fluctuations are shifted to longer times when lumping an amount of material smaller than a track, as their activation will be postponed as ensured by time consistency. Increasing the patches' dimensions will cause a noticeable reduction in computation times according to a linear trend (Fig. 13c). The very high values of the RMSE are further proof of the low accuracy of models having a smaller number of patches, as expected. The analysis of cooling rates and melt pool evaluations (Fig. 14, with M3 mesh used) can be strongly affected by the lumping.

As reported in Fig. 13c, one could then find an ideal compromise between computational time and accuracy within models such as *T* or P2, where the material deposition follows a resolution below the layer lumping, with parts of it deposited in a sequential way as executed in SFH methods as well [25]. Further increases in the number of patches per track (hence, reducing the patch dimension) will bring minor modifications to the temperature history, compensated by a non-negligible linear increase in the computational time. Considering the M1 mesh used for this analysis, one could replicate the moving heat source method by depositing 48 patches per track having a width equal to the element one in the x-direction. Such a technique would surely give the most accurate model, but also an increase of the computational time of 48 times compared to the recommended model T, and of 24 times to model P2.

In Table 5, the models analyzed with different contact times are listed. Patches of the same size as the tracks are considered here (as done previously in model T). This is done to easily accommodate high values of Δt_{cont} within the deposition time of each patch, as an increased dimension of the patch brings an increased deposition time. Fig. 15a shows that the temperature–time curves are pretty much unaffected when changing the contact time duration, with the part building up the

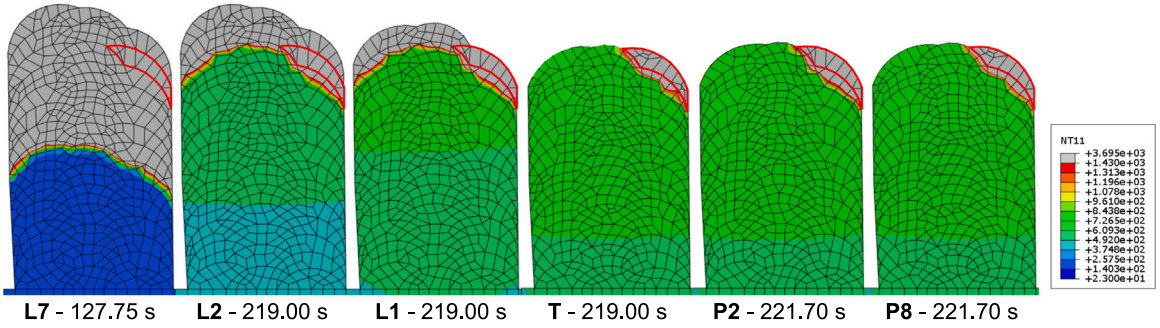

Fig. 14. Cross-section contour plots of the deposition when the middle of the first track of layer 13 gets deposited (highlighted in red). Deposition happens before when coarser patching is considered. The melt pool area is better predicted when patching is refined. The temperature unit is degrees Celsius. (For interpretation of the references to color in this figure legend, the reader is referred to the web version of this article.)

Table 5
Models analyzed for the parametric study on the contact time.

Model name	Δt_{cont} [s]
T1	5
T2	2
T3	1
T4	1e−1
T5	1e−2
T6	1e−3
T7	1e−4

temperature in a very similar way for all considered cases. However, by zooming in on the temperature–time curves shown in Fig. 15a it becomes evident that by increasing the heating time (while conserving the energy of course), temperature peaks are smoothened i.e. reaching lower temperatures, gradually resulting in GH rather than FH. This happens because employing longer contact times results in longer times for conduction of the heat within the component, even while this is still heating up, providing the decreased slope visualized in the curves. Such GH models will then have issues in the evaluation of cooling rates, as these depend on the curve slopes, and similarly for residual stresses in the case of thermomechanical models, as lower temperatures will underestimate the amount of plastic deformation introduced in the model. To distinguish between FH and GH models, Fig. 16 shows the melt pool size at the end of the heating phase of the first track deposited in the model. It is observed that for cases with higher contact times e.g. T1–T3 (GH), there is no sign of melt pool formation — signifying lower peak temperatures. While for shorter contact times (the FH case), e.g. T4–T7, almost the entire track cross-section has been melted. When calculating the contact time as in [28,29], the value for N would be 0.12 s, very close to the one tested in T4, which is a FH model. Based on the data shown Fig. 15b, it is possible to conclude that when a model is classified as FH it becomes basically insensitive to the Δt_{cont} value as the RMSE value shows (T7 used as a reference). In FH models, decreasing Δt_{cont} brings a slight increase in the run-time as the step size gets reduced, and the peak temperature of the molten phase is increased. The bulk temperature development is however insensitive to the contact time when in the FH range, resulting in the small values of RMSE recorded in Fig. 15b. The peak temperature evaluated in the FEM model should not be considered an accurate value, as the convective heat transfer in the melt pool is not included in the model. Given this, the calculated peak temperature is overestimated compared to experimental values reported in other studies with the same process and material [66]. Based on these results, the choice of the contact time should be related to the amount of molten volume detected in the simulation: a first guess can be estimated using the process parameters as done in [28,29], but this value should be further calibrated ensuring proper melting of the whole deposited volume. There is no advantage to directly using an extremely small value (e.g., 0.0001 s) as that would just be a disadvantage from a computational perspective. It should be emphasized that the advantage of using GH models is purely related to the short computational time, as the only reliable information that they provide is the *overall* build-up of the temperature in the part whilst ensuring energy conservation.

4.4. Comparison between process parameters

A parametric study is presented here using three sets of different process parameters (listed in Table 2) with a similar meshing as the one used for the validation for case N, resulting in 407 828 elements for L and 453 444 for H. This meshing is used to ensure proper prediction of the molten volume. Here, the P8 patching approach (i.e. division of a single track into 8 equal sections) is used, and a Δt_{cont} of 0.001 s is kept for every model to achieve FH. The calibrated values of ξ and h_{cool} obtained through validation of the case N in Section 4.1 are also kept for the new sets of process parameters.

In Fig. 17a, it is possible to see the temperature development at a probe predicted by the validated model, and it is clearly observed that the temperature curves differ substantially between the three cases. Sample L is deposited in way shorter times and with a smaller energy input due to a higher scanning speed, while sample H is made over a longer time and also has a higher energy input. For sample H, the temperature–time curve shows a saturation of heat accumulation: for the deposition of the final six layers ($t > 300$ s), the temperature does not increase anymore while building up a new layer. This is because the energy removed through convection/radiation from the surfaces gets balanced with the energy input given by $\dot{Q}'''$ due to the temperature difference between the surface and the ambient.

DED processes are known to present heat accumulation issues [12, 67]. These arise because the thermal energy provided in the previously printed layers does not dissipate enough through the geometry when new material gets deposited. One of the consequences of this is the increase in the melt pool size with the build height as the manufacturing process goes on [68]. An approach to evaluate the development of this molten volume with the build height is proposed here: from the simulation outputs, it is possible to highlight the regions showing a temperature above the melting point. The number of pixels occupied by such regions is then converted into an area measurement through Python code using the `skimage` package. For each track getting deposited, the maximum melting area is extracted at the middle of the track length in the x-direction.

Fig. 18 shows predicted cooling rates, molten area based on the method outlined above, as well as the experimental microhardness along the building height for the three different samples. The cooling rates are evaluated numerically by just taking the temperature–time data points located within T_{liq} and T_{sol}, for every node of interest. To evaluate the development of the cooling rate with the build height, one node in the middle of the second track of every layer is analyzed. While building up new layers, both the hardness and cooling rates tend

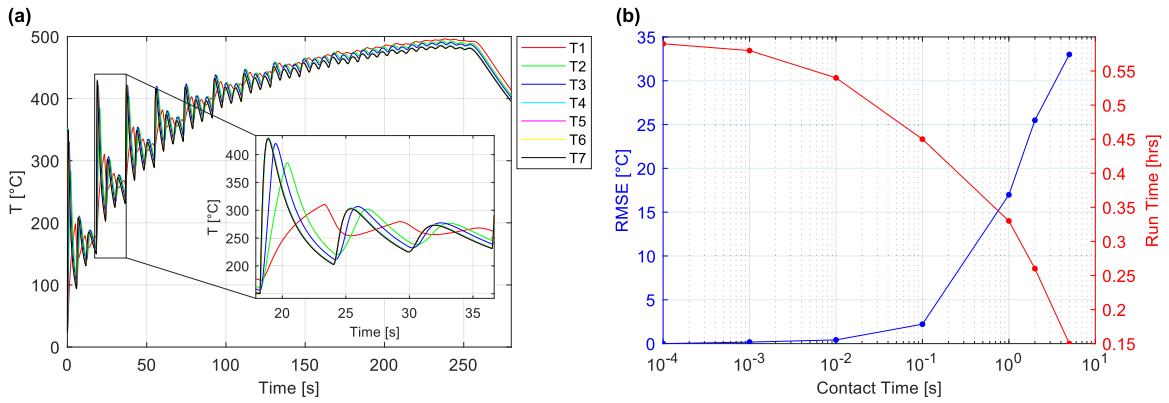

Fig. 15. (a) Temperature–time curves at the thermocouple position for models having different contact times. (b) RMSE and run time development with increasing contact time.

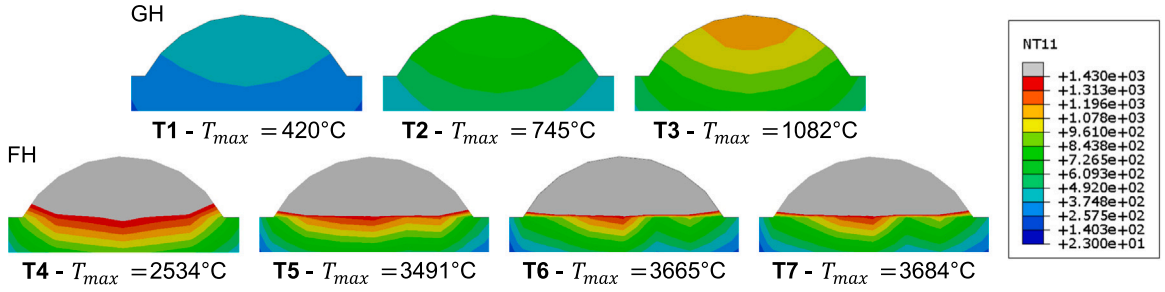

Fig. 16. Cross-section contour plots in the middle of the first track. For each model, the contour at the end of the contact time is shown (when all the thermal energy is provided and the maximum temperature T_{max} for each model is reached). The temperature unit is degrees Celsius.

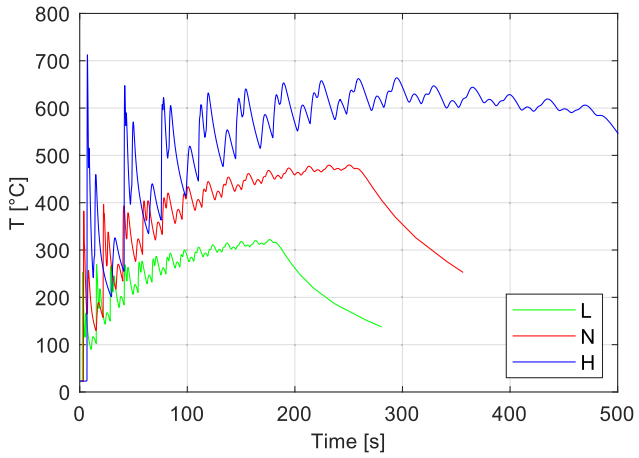

Fig. 17. Temperature–time curves at the thermocouple position for different process parameters.

to decrease accordingly [16,69], while the cross-sectional melting area detected increases. All of these effects are related to heat accumulation, since it takes more time to cool down every newly built layer as the temperature difference between the current and the previously deposited one is decreased. Lower cooling rates bring coarser grain size, which in turn results in a reduction in the hardness values [15]. At the same time, when the previously-built layer is still warm during the deposition of the new one, less energy is required to re-melt it, and given the constant energy input for all of the patches, the amount of material that will undergo melting increases layer after layer.

When comparing different process parameters, lower energy densities result in higher hardness and cooling rates, while the melting areas are smaller.

One should also notice that the values of the melting area are always above the deposited one for both samples N and H, while this is not the case for sample L, which for the first four layers has values very close to or below the deposited area (1.3 mm^2). This is reflected experimentally in lack-of-fusion porosities, see Fig. 19a. These are characterized by an irregular shape and are located along a vertical line in the overlapping between the two neighbor tracks, which probably means that the overlapping is not sufficient for this level of energy input. The fact that sample L is the only one showing such defects and also having the numerical model not fully melting the tracks for the first layers allow us to conclude that the thermal model can predict whether the thermal input of the laser is high enough to melt the material planned to be deposited fully. The increased melt pool area with the distance from the baseplate proves that remelting of previous layers is enhanced with the building height, explaining why the samples after etching in Figs. 4 and 5 show bigger areas for the last layers. Always in the same as-built micrographs, an increasing amount of spherical oxide inclusions with a diameter below 10 μm is found when the energy density increases (Fig. 19b). As confirmed by EDS analysis and according to [70,71], these are Si(Al) and Mn-rich oxide inclusions ranging from 500 nm to 10 μm. Cracks at the surface are found in the three samples (here visualized only in the micrograph of sample N, see Fig. 19a). These could be caused by hot cracking and promoted by the presence of oxide inclusions [71,72].

Cooling rates between 1600–3500 °C/s have been measured in other studies for DED of 316L with decreasing values when increasing build height [11,13,73,74]. These values are above what was found with samples N and H. However, samples produced with energy densities below 120 J/mm are analyzed in these studies, meaning that values below 1600 °C/s should be expected for the higher energy density samples. The difference between the cooling rates of the different samples is reflected in the microstructure (Fig. 19c): the microstructural evolution goes from a fine equiaxed grain morphology (sample L) to coarse column grains (sample H). Similar microstructures are also

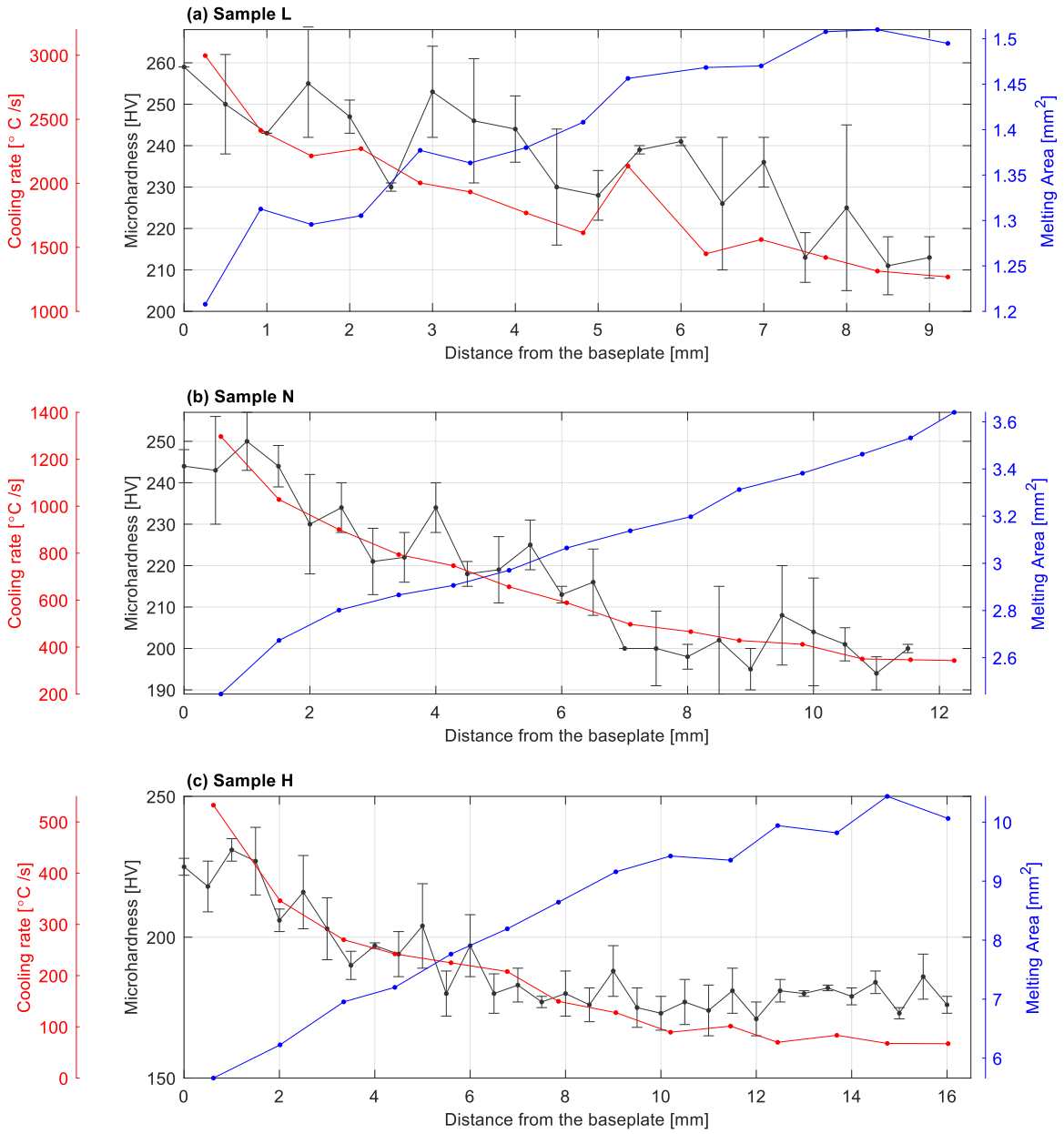

Fig. 18. Microhardness (experimental), cooling rates (numerical), and cross-sectional melting areas (numerical) analyzed through the deposited height for sample L (a), N (b), and H (c).

found in [75]. According to [76], an increase in the cooling rate leads to a microstructure refinement. The transition from equiaxed to columnar grains is instead due to low solidification rates.

The saturation of the heat accumulation for sample H can once again be noticed by the almost constant microhardness and cooling rates when the distance from the baseplate is bigger than 10 mm, corresponding to the final six layers. As a final check on this, Appendix B provides a collection of pictures obtained by the in-axis thermal camera installed during the production. While for both samples L and N the radiation intensity always increases with the layer number from the first to the final one, for sample H this increase is not noticed for the upper layers above layer five. We also notice the previously mentioned improper melting of the first layers of sample L, as the area covered by the laser diameters is not homogeneously heated up, and that the tail behind gets bigger with increased energy density and layer number, proving the increase of melt pool volume with the number of layers and energy density.

5. Conclusion

This work presents a new procedure for applying the FH method to DED processes in which the thermal input given by the laser is evaluated through the process parameters and the cross-sectional area of a single-track deposition. The model has been validated through monitoring data from experiments and applied to different sets of process parameters. The following conclusions can be made:

- The FH method effectively replicates experimental results within short computational times. The implementation of computational fluid dynamics-based thermal models for the same purpose obviously would provide more accurate results in terms of geometry, fluid motion, and heat transfer. However, its application to multi-layer geometries would result in excessively high computational times.
- Implementation of high-fidelity geometries based on OM pictures gives a reliable evaluation of cooling rates and development of

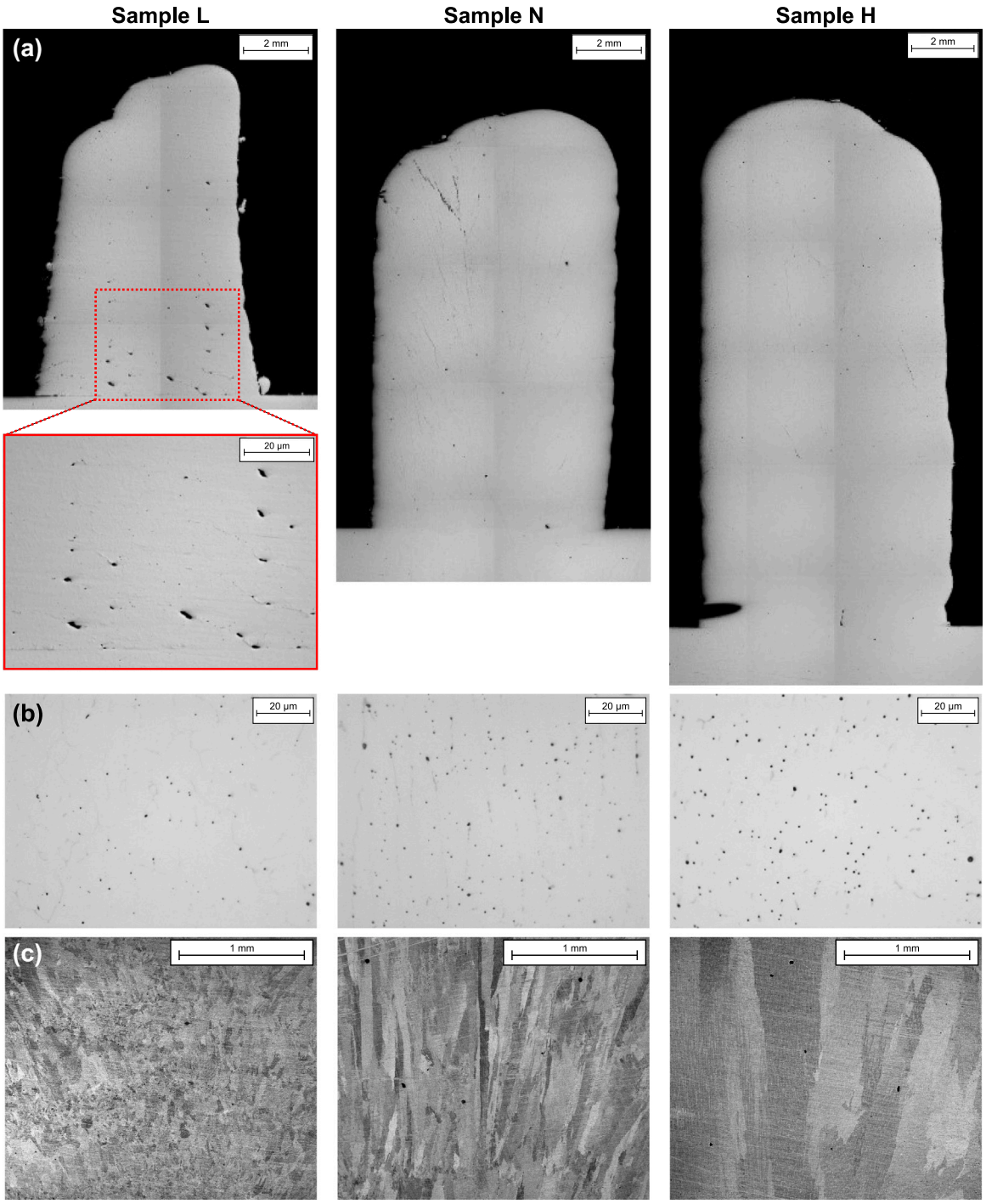

Fig. 19. (a) OM of the as-built samples cross-sections. (b) OM of the samples magnified to visualize oxide inclusions. Images taken at the middle of the build height. (c) SEM micrographs acquired using back-scattered electrons detectors. ECCI mode is used to distinguish the orientation of the grains. Images taken at the middle of the build height.

the melt pool areas during the deposition of layers. The former can be used to investigate microstructure outputs and the latter to evaluate eventual lack-of-fusion porosities or remelting of previous layers. The curvilinear surfaces composing the cross-sectional areas of the tracks have been manually drawn. However, we envision the possibility of using an algorithm doing so, capable of developing a high-fidelity representation of the multi-layer geometry given the values of laser diameter, hatch spacing, and cross-sectional area of a single-track experiment. Furthermore, the single-track experiment does not have to be executed for any set of process parameters: once two single-track experiments have been executed with process parameters providing low and high energy densities, the areas of tracks with energy density values in between can be evaluated through linear interpolation as an approximation. The feasibility of this framework should be evaluated in future work.

- When increasing the dimensions of the patches, the computational times can be shortened even more, however with increased loss of information from a thermal perspective. Cooling rates and molten volume evaluations are becoming increasingly more inaccurate, however, the model might still be useful for a subsequent thermomechanical analysis and hence provide useful information. Further evaluations of this should be made.

- The contact time value defines whether the model is in FH or GH mode. If this value is high enough not to generate any melt pool, then the model can be classified as GH: in which case, reliable overall temperature build-up information is still provided, but cooling rates, melt pool, and subsequent thermomechanical evaluations could be inaccurate.
- DED samples are characterized by heat accumulation when building up several layers. It is possible to reach saturation when a high energy density is input into the sample, as the heat extraction eventually gets balanced with the input. This has been verified both with experimental and numerical results.

Future work should be tailored to the application of the proposed FH formulation to thermomechanical models, to evaluate the influence of simulation parameters on residual stresses and deformations. However, the relatively low computational cost of the thermal part of the FH method is expected to be increased substantially from adding the mechanical analysis, and attention should be paid to coping with this.

CRediT authorship contribution statement

Alberto Santi: Conceptualization, Data curation, Formal analysis, Investigation, Methodology, Visualization, Writing – original draft. **Mohamad Bayat:** Conceptualization, Investigation, Methodology, Supervision, Writing – review & editing. **Venkata Karthik Nadimpalli:** Investigation, Methodology. **Alberto Fabrizi:** Data curation, Investigation. **Franco Bonollo:** Investigation, Supervision. **Jesper Henri Hattel:** Conceptualization, Funding acquisition, Writing – review & editing.

Declaration of competing interest

The authors declare the following financial interests/personal relationships which may be considered as potential competing interests: Mohamad Bayat reports financial support was provided by Technical University of Denmark. Jesper Henri Hattel reports financial support was provided by Technical University of Denmark. If there are other authors, they declare that they have no known competing financial interests or personal relationships that could have appeared to influence the work reported in this paper.

Acknowledgments

AS received funding from the Technical University of Denmark (DTU). MB and JH received funding from Independent Research Fund Denmark, DIGI-3D project (Contract No. 0136–00210B).

Appendix A. Supplementary data

Supplementary material related to this article can be found online at https://doi.org/10.1016/j.jmapro.2024.05.026.

References

[1] Gisario A, Kazarian M, Martina F, Mehrpouya M. Metal additive manufacturing in the commercial aviation industry: A review. J Manuf Syst 2019;53:124–49. http://dx.doi.org/10.1016/j.jmsy.2019.08.005.

[2] DebRoy T, Wei HL, Zuback JS, Mukherjee T, Elmer JW, Milewski JO, Beese AM, Wilson-Heid A, De A, Zhang W. Additive manufacturing of metallic components – Process, structure and properties. Prog Mater Sci 2018;92:112–224. http://dx.doi.org/10.1016/j.pmatsci.2017.10.001.

[3] Everton SK, Hirsch M, Stravroulakis P, Leach RK, Clare AT. Review of in-situ process monitoring and in-situ metrology for metal additive manufacturing. Mater Des 2016;95:431–45. http://dx.doi.org/10.1016/j.matdes.2016.01.099.

[4] Rankouhi B, Bertsch KM, Meric de Bellefon G, Thevamaran M, Thoma DJ, Suresh K. Experimental validation and microstructure characterization of topology optimized, additively manufactured SS316L components. Mater Sci Eng A 2020;776:139050. http://dx.doi.org/10.1016/j.msea.2020.139050.

[5] Francois MM, Sun A, King WE, Henson NJ, Tourret D, Bronkhorst CA, Carlson NN, Newman CK, Haut T, Bakosi J, Gibbs JW, Livescu V, Vander Wiel SA, Clarke AJ, Schraad MW, Blacker T, Lim H, Rodgers T, Owen S, Abdeljawad F, Madison J, Anderson AT, Fattebert J-L, Ferencz RM, Hodge NE, Khairallah SA, Walton O. Modeling of additive manufacturing processes for metals: Challenges and opportunities. Curr Opin Solid State Mater Sci 2017;21(4):198–206. http://dx.doi.org/10.1016/j.cossms.2016.12.001.

[6] Yan Z, Liu W, Tang Z, Liu X, Zhang N, Li M, Zhang H. Review on thermal analysis in laser-based additive manufacturing. Opt Laser Technol 2018;106:427–41. http://dx.doi.org/10.1016/j.optlastec.2018.04.034.

[7] Thompson SM, Bian L, Shamsaei N, Yadollahi A. An overview of Direct Laser Deposition for additive manufacturing; Part I: Transport phenomena, modeling and diagnostics. Addit Manuf 2015;8:36–62. http://dx.doi.org/10.1016/j.addma.2015.07.001.

[8] Bayat M, Dong W, Thorborg J, To AC, Hattel JH. A review of multi-scale and multi-physics simulations of metal additive manufacturing processes with focus on modeling strategies. Addit Manuf 2021;47:102278. http://dx.doi.org/10.1016/j.addma.2021.102278.

[9] Nie P, Ojo OA, Li Z. Numerical modeling of microstructure evolution during laser additive manufacturing of a nickel-based superalloy. Acta Mater 2014;77:85–95. http://dx.doi.org/10.1016/j.actamat.2014.05.039.

[10] Bayat M, Nadimpalli VK, Biondani FG, Jafarzadeh S, Thorborg J, Tiedje NS, Bissacco G, Pedersen DB, Hattel JH. On the role of the powder stream on the heat and fluid flow conditions during Directed Energy Deposition of maraging steel—Multiphysics modeling and experimental validation. Addit Manuf 2021;43:102021. http://dx.doi.org/10.1016/j.addma.2021.102021.

[11] Fetni S, Enrici TM, Niccolini T, Tran HS, Dedry O, Duchêne L, Mertens A, Habraken AM. Thermal model for the directed energy deposition of composite coatings of 316L stainless steel enriched with tungsten carbides. Mater Des 2021;204:109661. http://dx.doi.org/10.1016/j.matdes.2021.109661.

[12] Chaudry MA, Mohr G, Hilgenberg K. Experimental and numerical comparison of heat accumulation during laser powder bed fusion of 316L stainless steel. Prog Addit Manuf 2022;7(5):1071–83. http://dx.doi.org/10.1007/s40964-022-00282-x.

[13] Park J, Kim J-y, Ji I, Lee SH. Numerical and experimental investigations of laser metal deposition (LMD) using STS 316L. Appl Sci 2020;10(14):4874. http://dx.doi.org/10.3390/app10144874, Number: 14 Publisher: Multidisciplinary Digital Publishing Institute.

[14] Chiumenti M, Neiva E, Salsi E, Cervera M, Badia S, Moya J, Chen Z, Lee C, Davies C. Numerical modelling and experimental validation in Selective Laser Melting. Addit Manuf 2017;18:171–85. http://dx.doi.org/10.1016/j.addma.2017.09.002.

[15] Zuback JS, DebRoy T. The hardness of additively manufactured alloys. Materials 2018;11(11):2070. http://dx.doi.org/10.3390/ma11112070, Number: 11 Publisher: Multidisciplinary Digital Publishing Institute.

[16] Moheimani SK, Iuliano L, Saboori A. The role of substrate preheating on the microstructure, roughness, and mechanical performance of AISI 316L produced by directed energy deposition additive manufacturing. Int J Adv Manuf Technol 2022;119(11):7159–74. http://dx.doi.org/10.1007/s00170-021-08564-4.

[17] Santi A, Bayat M, Hattel J. Multiphysics modeling of metal based additive manufacturing processes with focus on thermomechanical conditions. J Therm Stresses 2023;46(6):445–63. http://dx.doi.org/10.1080/01495739.2023.2195513.

[18] Zhang W, Tong M, Harrison NM. Resolution, energy and time dependency on layer scaling in finite element modelling of laser beam powder bed fusion additive manufacturing. Addit Manuf 2019;28:610–20. http://dx.doi.org/10.1016/j.addma.2019.05.002.

[19] Denlinger ER, Irwin J, Michaleris P. Thermomechanical modeling of additive manufacturing large parts. J Manuf Sci Eng 2014;136(061007). http://dx.doi.org/10.1115/1.4028669.

[20] Bailey NS, Katinas C, Shin YC. Laser direct deposition of AISI H13 tool steel powder with numerical modeling of solid phase transformation, hardness, and residual stresses. J Mater Process Technol 2017;247:223–33. http://dx.doi.org/10.1016/j.jmatprotec.2017.04.020.

[21] Wang J, Zhang J, Liu G, Liang L, Yang G, Huang A, Pang S. Effects of scanning strategies on residual stress and deformation by high-power direct energy deposition: Island size and laser jump strategy between islands. J Manuf Process 2022;75:23–40. http://dx.doi.org/10.1016/j.jmapro.2021.12.054.

[22] Heigel JC, Michaleris P, Reutzel EW. Thermo-mechanical model development and validation of directed energy deposition additive manufacturing of Ti–6Al–4V. Addit Manuf 2015;5:9–19. http://dx.doi.org/10.1016/j.addma.2014.10.003.

[23] Hodge NE, Ferencz RM, Vignes RM. Experimental comparison of residual stresses for a thermomechanical model for the simulation of selective laser melting. Addit Manuf 2016;12:159–68. http://dx.doi.org/10.1016/j.addma.2016.05.011.

[24] Dong W, Jimenez XA, To AC. Temperature-dependent modified inherent strain method for predicting residual stress and distortion of Ti6Al4V walls manufactured by wire-arc directed energy deposition. Addit Manuf 2023;62:103386. http://dx.doi.org/10.1016/j.addma.2022.103386.

[25] Bayat M, Klingaa CG, Mohanty S, De Baere D, Thorborg J, Tiedje NS, Hattel JH. Part-scale thermo-mechanical modelling of distortions in Laser Powder Bed Fusion – Analysis of the sequential flash heating method with experimental validation. Addit Manuf 2020;36:101508. http://dx.doi.org/10.1016/j.addma.2020.101508.

[26] Afazov S, Okioga A, Holloway A, Denmark W, Triantaphyllou A, Smith S-A, Bradley-Smith L. A methodology for precision additive manufacturing through compensation. Precis Eng 2017;50:269–74. http://dx.doi.org/10.1016/j.precisioneng.2017.05.014.

[27] De Baere D, Van Cauwenbergh P, Bayat M, Mohanty S, Thorborg J, Thijs L, Van Hooreweder B, Vanmeensel K, Hattel JH. Thermo-mechanical modelling of stress relief heat treatments after laser-based powder bed fusion. Addit Manuf 2021;38:101818. http://dx.doi.org/10.1016/j.addma.2020.101818.

[28] Wang J, Zhang J, Liang L, Huang A, Yang G, Pang S. A line-based flash heating method for numerical modeling and prediction of directed energy deposition manufacturing process. J Manuf Process 2022;73:822–38. http://dx.doi.org/10.1016/j.jmapro.2021.11.041.

[29] Li C, Liu JF, Guo YB. Prediction of residual stress and part distortion in selective laser melting. Procedia CIRP 2016;45:171–4. http://dx.doi.org/10.1016/j.procir.2016.02.058.

[30] Mohanty S, Hattel J. Cellular scanning strategy for selective laser melting: Capturing thermal trends with a low-fidelity, pseudo-analytical model. Math Probl Eng 2014;2014:e715058. http://dx.doi.org/10.1155/2014/715058, Publisher: Hindawi.

[31] Roberts IA, Wang CJ, Esterlein R, Stanford M, Mynors DJ. A three-dimensional finite element analysis of the temperature field during laser melting of metal powders in additive layer manufacturing. Int J Mach Tools Manuf 2009;49(12):916–23. http://dx.doi.org/10.1016/j.ijmachtools.2009.07.004.

[32] Michaleris P. Modeling metal deposition in heat transfer analyses of additive manufacturing processes. Finite Elem Anal Des 2014;86:51–60. http://dx.doi.org/10.1016/j.finel.2014.04.003.

[33] Hodge NE, Ferencz RM, Solberg JM. Implementation of a thermomechanical model for the simulation of selective laser melting. Comput Mech 2014;54(1):33–51. http://dx.doi.org/10.1007/s00466-014-1024-2.

[34] Liu Y, Zhang J, Pang Z. Numerical and experimental investigation into the subsequent thermal cycling during selective laser melting of multi-layer 316L stainless steel. Opt Laser Technol 2018;98:23–32. http://dx.doi.org/10.1016/j.optlastec.2017.07.034.

[35] Yang Q, Zhang P, Cheng L, Min Z, Chyu M, To AC. Finite element modeling and validation of thermomechanical behavior of Ti-6Al-4V in directed energy deposition additive manufacturing. Addit Manuf 2016;12:169–77. http://dx.doi.org/10.1016/j.addma.2016.06.012.

[36] Goldak J, Chakravarti A, Bibby M. A new finite element model for welding heat sources. Metall Trans B 1984;15(2):299–305. http://dx.doi.org/10.1007/BF02667333.

[37] Gusarov AV, Yadroitsev I, Bertrand P, Smurov I. Model of radiation and heat transfer in laser-powder interaction zone at selective laser melting. J Heat Transfer 2009;131(072101). http://dx.doi.org/10.1115/1.3109245.

[38] Gouge M, Denlinger E, Irwin J, Li C, Michaleris P. Experimental validation of thermo-mechanical part-scale modeling for laser powder bed fusion processes. Addit Manuf 2019;29:100771. http://dx.doi.org/10.1016/j.addma.2019.06.022.

[39] Olleak A, Dugast F, Bharadwaj P, Strayer S, Hinnebusch S, Narra S, To AC. Enabling Part-Scale Scanwise process simulation for predicting melt pool variation in LPBF by combining GPU-based Matrix-free FEM and adaptive Remeshing. Addit Manuf Lett 2022;3:100051. http://dx.doi.org/10.1016/j.addlet.2022.100051.

[40] Burkhardt C, Steinmann P, Mergheim J. Thermo-mechanical simulations of powder bed fusion processes: accuracy and efficiency. Adv Model Simul Eng Sci 2022;9(1):18. http://dx.doi.org/10.1186/s40323-022-00230-y.

[41] Zaeh MF, Branner G. Investigations on residual stresses and deformations in selective laser melting. Prod Eng 2010;4(1):35–45. http://dx.doi.org/10.1007/s11740-009-0192-y.

[42] Ueda Y, Fukuda K, Nakacho K, Endo S. A new measuring method of residual stresses with the aid of finite element method and reliability of estimated values. J Soc Nav Archit Jpn 1975;1975(138):499–507. http://dx.doi.org/10.2534/jjasnaoe1968.1975.138_499.

[43] Liang X, Cheng L, Chen Q, Yang Q, To AC. A modified method for estimating inherent strains from detailed process simulation for fast residual distortion prediction of single-walled structures fabricated by directed energy deposition. Addit Manuf 2018;23:471–86. http://dx.doi.org/10.1016/j.addma.2018.08.029.

[44] Liang X, Chen Q, Cheng L, Hayduke D, To AC. Modified inherent strain method for efficient prediction of residual deformation in direct metal laser sintered components. Comput Mech 2019;64(6):1719–33. http://dx.doi.org/10.1007/s00466-019-01748-6.

[45] Ye R, Smugeresky JE, Zheng B, Zhou Y, Lavernia EJ. Numerical modeling of the thermal behavior during the LENS® process. Mater Sci Eng A 2006;428(1):47–53. http://dx.doi.org/10.1016/j.msea.2006.04.079.

[46] Denlinger ER, Michaleris P. Effect of stress relaxation on distortion in additive manufacturing process modeling. Addit Manuf 2016;12:51–9. http://dx.doi.org/10.1016/j.addma.2016.06.011.

[47] Neela V, De A. Three-dimensional heat transfer analysis of LENSTM process using finite element method. Int J Adv Manuf Technol 2009;45(9):935–43. http://dx.doi.org/10.1007/s00170-009-2024-9.

[48] Sampson R, Lancaster R, Sutcliffe M, Carswell D, Hauser C, Barras J. The influence of key process parameters on melt pool geometry in direct energy deposition additive manufacturing systems. Opt Laser Technol 2021;134:106609. http://dx.doi.org/10.1016/j.optlastec.2020.106609.

[49] Nikam S, Wu H, Harkin R, Quinn J, Lupoi R, Yin S, McFadden S. On the application of the anisotropic enhanced thermal conductivity approach to thermal modelling of laser-based powder bed fusion processes. Addit Manuf 2022;55:102870. http://dx.doi.org/10.1016/j.addma.2022.102870.

[50] Caiazzo F, Alfieri V. Simulation of laser-assisted directed energy deposition of aluminum powder: Prediction of geometry and temperature evolution. Materials 2019;12(13):2100. http://dx.doi.org/10.3390/ma12132100, Number: 13 Publisher: Multidisciplinary Digital Publishing Institute.

[51] dos Santos Paes LE, Ferreira HS, Pereira M, Xavier FA, Weingaertner WL, Vilarinho LO. Modeling layer geometry in directed energy deposition with laser for additive manufacturing. Surf Coat Technol 2021;409:126897. http://dx.doi.org/10.1016/j.surfcoat.2021.126897.

[52] Ocelík V, Nenadl O, Palavra A, De Hosson JTM. On the geometry of coating layers formed by overlap. Surf Coat Technol 2014;242:54–61. http://dx.doi.org/10.1016/j.surfcoat.2014.01.018.

[53] Nenadl O, Kuipers W, Koelewijn N, Ocelík V, De Hosson JTM. A versatile model for the prediction of complex geometry in 3D direct laser deposition. Surf Coat Technol 2016;307:292–300. http://dx.doi.org/10.1016/j.surfcoat.2016.08.090.

[54] Huang Y, Khamesee MB, Toyserkani E. A new physics-based model for laser directed energy deposition (powder-fed additive manufacturing): From single-track to multi-track and multi-layer. Opt Laser Technol 2019;109:584–99. http://dx.doi.org/10.1016/j.optlastec.2018.08.015.

[55] Ansari M, Martinez-Marchese A, Khamooshi M, Keshavarzkermani A, Esmaeilizadeh R, Toyserkani E. Analytical modeling of multi-track powder-fed laser directed energy deposition: On the relationships among process, deposition dimensions, and solidification microstructure in additively manufactured near-beta titanium alloy. J Mater Process Technol 2022;306:117643. http://dx.doi.org/10.1016/j.jmatprotec.2022.117643.

[56] AghaAli I, Farzam M, Golozar MA, Danaee I. The effect of repeated repair welding on mechanical and corrosion properties of stainless steel 316L. Mater Des (1980-2015) 2014;54:331–41. http://dx.doi.org/10.1016/j.matdes.2013.08.052.

[57] Liu ZW, Lin CC, Jiang CF, Hua JJ, Zhang JM, Zeng Y. Analysis of electron channeling contrast imaging in scanning electron microscopes. Key Eng Mater 2018;768:52–8. http://dx.doi.org/10.4028/www.scientific.net/KEM.768.52, Publisher: Trans Tech Publications Ltd.

[58] MAGMASOFT® Material Database.

[59] Partes K. Analytical model of the catchment efficiency in high speed laser cladding. Surf Coat Technol 2009;204(3):366–71. http://dx.doi.org/10.1016/j.surfcoat.2009.07.041.

[60] Wen SY, Shin YC, Murthy JY, Sojka PE. Modeling of coaxial powder flow for the laser direct deposition process. Int J Heat Mass Transfer 2009;52(25):5867–77. http://dx.doi.org/10.1016/j.ijheatmasstransfer.2009.07.018.

[61] Wu Y-C, San C-H, Chang C-H, Lin H-J, Marwan R, Baba S, Hwang W-S. Numerical modeling of melt-pool behavior in selective laser melting with random powder distribution and experimental validation. J Mater Process Technol 2018;254:72–8. http://dx.doi.org/10.1016/j.jmatprotec.2017.11.032.

[62] Lee YS, Zhang W. Modeling of heat transfer, fluid flow and solidification microstructure of nickel-base superalloy fabricated by laser powder bed fusion. Addit Manuf 2016;12:178–88. http://dx.doi.org/10.1016/j.addma.2016.05.003.

[63] Khairallah SA, Anderson AT, Rubenchik A, King WE. Laser powder-bed fusion additive manufacturing: Physics of complex melt flow and formation mechanisms of pores, spatter, and denudation zones. Acta Mater 2016;108:36–45. http://dx.doi.org/10.1016/j.actamat.2016.02.014.

[64] Figueredo EWA, Apolinario LHR, Santos MV, Silva ACS, Avila JA, Lima MSF, Santos TFA. Influence of laser beam power and scanning speed on the macrostructural characteristics of AISI 316L and AISI 431 stainless steel depositions produced by laser cladding process. J Mater Eng Perform 2021;30(5):3298–312. http://dx.doi.org/10.1007/s11665-021-05676-6.

[65] Yan J, Zhou Y, Gu R, Zhang X, Quach W-M, Yan M. A comprehensive study of steel powders (316L, H13, P20 and 18Ni300) for their selective laser melting additive manufacturing. Metals 2019;9(1):86. http://dx.doi.org/10.3390/met9010086, Number: 1 Publisher: Multidisciplinary Digital Publishing Institute.

[66] Smoqi Z, Bevans BD, Gaikwad A, Craig J, Abul-Haj A, Roeder B, Macy B, Shield JE, Rao P. Closed-loop control of meltpool temperature in directed energy deposition. Mater Des 2022;215:110508. http://dx.doi.org/10.1016/j.matdes.2022.110508.

[67] Hagenlocher C, O'Toole P, Xu W, Brandt M, Easton M, Molotnikov A. Analytical modelling of heat accumulation in laser based additive manufacturing processes of metals. Addit Manuf 2022;60:103263. http://dx.doi.org/10.1016/j.addma.2022.103263.

[68] Zheng B, Haley JC, Yang N, Yee J, Terrassa KW, Zhou Y, Lavernia EJ, Schoenung JM. On the evolution of microstructure and defect control in 316L SS components fabricated via directed energy deposition. Mater Sci Eng A 2019;764:138243. http://dx.doi.org/10.1016/j.msea.2019.138243.

[69] Chechik L, Christofidou KA, Markanday JFS, Goodall AD, Miller JR, West G, Stone H, Todd I. Hardness variation in inconel 718 produced by laser directed energy deposition. Materialia 2022;26:101643. http://dx.doi.org/10.1016/j.mtla.2022.101643.

[70] Saboori A, Piscopo G, Lai M, Salmi A, Biamino S. An investigation on the effect of deposition pattern on the microstructure, mechanical properties and residual stress of 316L produced by Directed Energy Deposition. Mater Sci Eng A 2020;780:139179. http://dx.doi.org/10.1016/j.msea.2020.139179.

[71] Lou X, Andresen PL, Rebak RB. Oxide inclusions in laser additive manufactured stainless steel and their effects on impact toughness and stress corrosion cracking behavior. J Nucl Mater 2018;499:182–90. http://dx.doi.org/10.1016/j.jnucmat.2017.11.036.

[72] Xu K, Li B, Jiang C. Adjusting microstructure and improving mechanical property of additive manufacturing 316L based on process optimization. Mater Sci Eng A 2023;870:144824. http://dx.doi.org/10.1016/j.msea.2023.144824.

[73] Amine T, Newkirk JW, Liou F. Investigation of effect of process parameters on multilayer builds by direct metal deposition. Appl Therm Eng 2014;73(1):500–11. http://dx.doi.org/10.1016/j.applthermaleng.2014.08.005.

[74] Mukherjee T, Manvatkar V, De A, DebRoy T. Dimensionless numbers in additive manufacturing. J Appl Phys 2017;121(6):064904. http://dx.doi.org/10.1063/1.4976006.

[75] Pacheco JT, Meura VH, Bloemer PRA, Veiga MT, de Moura Filho OC, Cunha A, Teixeira MF. Laser directed energy deposition of AISI 316L stainless steel: The effect of build direction on mechanical properties in as-built and heat-treated conditions. Adv Ind Manuf Eng 2022;4:100079. http://dx.doi.org/10.1016/j.aime.2022.100079.

[76] Bontha S, Klingbeil NW, Kobryn PA, Fraser HL. Thermal process maps for predicting solidification microstructure in laser fabrication of thin-wall structures. J Mater Process Technol 2006;178(1):135–42. http://dx.doi.org/10.1016/j.jmatprotec.2006.03.155.